



**HAL**  
open science

## Chiral diketopyrrolopyrrole dyes showing light emission in solid and aggregate states

Maurizio Mastropasqua Talamo, Thomas Cauchy, Flavia Pop, Francesco  
Zinna, Lorenzo Di Bari, Narcis Avarvari

► **To cite this version:**

Maurizio Mastropasqua Talamo, Thomas Cauchy, Flavia Pop, Francesco Zinna, Lorenzo Di Bari, et al.. Chiral diketopyrrolopyrrole dyes showing light emission in solid and aggregate states. *Journal of Materials Chemistry C*, 2023, 11 (17), pp.5701-5713. 10.1039/D3TC00308F . hal-04240759

**HAL Id: hal-04240759**

**<https://hal.science/hal-04240759>**

Submitted on 15 Nov 2023

**HAL** is a multi-disciplinary open access archive for the deposit and dissemination of scientific research documents, whether they are published or not. The documents may come from teaching and research institutions in France or abroad, or from public or private research centers.

L'archive ouverte pluridisciplinaire **HAL**, est destinée au dépôt et à la diffusion de documents scientifiques de niveau recherche, publiés ou non, émanant des établissements d'enseignement et de recherche français ou étrangers, des laboratoires publics ou privés.

# Chiral diketopyrrolopyrrole dyes with light emission from solid and aggregate states

Maurizio Mastropasqua Talamo,<sup>\*a</sup> Thomas Cauchy,<sup>a</sup> Flavia Pop,<sup>\*a</sup> Francesco Zinna,<sup>b</sup> Lorenzo Di Bari<sup>b</sup> and Narcis Avarvari<sup>\*a</sup>

<sup>a</sup> *Univ Angers, CNRS, MOLTECH-Anjou, SFR MATRIX, F-49000 Angers, France.*

<sup>b</sup> *Dipartimento di Chimica e Chimica Industriale, Università di Pisa, via G. Moruzzi 13, 56124, Pisa, Italy.*

E-mail: [maurizio.mastropasquatalamo@univ-angers.fr](mailto:maurizio.mastropasquatalamo@univ-angers.fr); [flavia.pop@univ-angers.fr](mailto:flavia.pop@univ-angers.fr); [narcis.avarvari@univ-angers.fr](mailto:narcis.avarvari@univ-angers.fr)

## Abstract

Due to their excellent emissive properties in solution, diketopyrrolo[3,4-*c*]pyrrole (DPP) derivatives are expected to show interesting features in the emission from the solid state by suppressing the aggregation-caused quenching. In this work, aggregation-enhanced emission (AEE) and circularly-polarised light (CPL) emission from the aggregate state have been studied on achiral and chiral DPPs appended with tetraarylethylene units. Both thiophene and phenyl DPPs (**2** and **5**) show the classical aggregation-caused quenching (ACQ) of the emission behaviour in the solid state, whereas the presence of triphenylethylene units (**3** and **6**) does not completely quench the emission in the solution. Nevertheless, enhancement of the emission from the solution to solid state films from 25 to 36% is observed with phenyl DPP (**3**) whereas the less distorted thiophene analogue **6** still shows the classical ACQ behaviour. When the photoluminescence behaviour of the aggregate states was studied in a series of THF/water mixtures, phenyl DPP **3** shows a 2-fold enhancement of the fluorescence intensity when the water fraction increases from 0% up to 70%, accompanied by an increase of the quantum yield from 17% up to 28%, and the achiral compound **8** shows a 3.5-fold enhancement of the fluorescence intensity when the water fraction increases from 0% to 50%, accompanied by an increase of the quantum yield from 20% up to 58%. Alkylation of DPPs by Mitsunobu reaction with *N*-*sec*-phenethyl groups have the advantage to increase the chiroptical properties in solution due to the proximity of the stereogenic motif. Thus, compound **3**, dissolved at concentration of  $10^{-6}$  M in  $\text{CHCl}_3$ , emitted detectable CPL under excitation at 365 nm, with  $|g_{\text{lum}}|$  around  $2 \times 10^{-4}$ , with positive values for the *SS* enantiomer and negative for *RR*. In this work, we show the importance of the position of the stereogenic motif within the chiral unit and the steric demand of the tetraarylethylene motifs needed to induce light emission in the solid state and CPL emission of chiroptical materials based on DPPs.

## 1. Introduction

Molecular and polymeric  $\pi$ -conjugated organic materials are key components in the development of organic electronic devices such as systems for energy harvesting, light emitting diodes (OLEDs) and transistors (OFETs).<sup>1-5</sup> The advantages of using organic compounds in these optoelectronic technologies include relatively low costs of fabrication, easy processing,

and the tunability of the optoelectronic properties (optical absorption, radiative and/or non-radiative relaxation, exciton diffusion, charge transport) by tailoring the molecular structures and directing the supramolecular organization, *via* expedient chemical synthesis.<sup>6-10</sup> The introduction of molecular chirality into organic optoelectronic materials is recently receiving a considerable interest as it can help driving preferential packing modes in the solid state, and also because the interplay between chirality and optoelectronic features can generate chiroptical, magnetochiral and spin-selective properties which pave the way to a number of feasible innovative technologies ranging from cryptography, quantum photonics, three-dimensional imaging, chiral probes, stereoscopic and/or anti-glare displays with enhanced external efficiency.<sup>1, 11-15</sup>

Enantiopure chiral chromophores exhibit a differential interaction with the two modes of circular polarization of the light, namely the left and right Circularly Polarized (CP) light. The differential absorption of these two components results in electronic circular dichroism (ECD), and its measurement constitutes one of the main analytical techniques for the characterization of chiral compounds. ECD spectroscopy can indeed deliver precious information about the configurational and conformational composition of a sample, and its supramolecular organization.<sup>16-18</sup> In case of radiative relaxation from an excited state, left and right polarizations are emitted differently, which amounts to circularly polarized luminescence or CPL. CPL can be quantified by the dissymmetry factor defined as  $g_{lum} = 2(I_L - I_R)/(I_L + I_R)$ , where  $I_L$  and  $I_R$  are the intensities of the left- and right-handed circularly polarised emitted lights, respectively.<sup>19, 20</sup> Moreover, another expedient metrics is CPL brightness ( $B_{CPL}$ ), which beside  $g_{lum}$  takes into account the extinction coefficient ( $\epsilon$ ) and the quantum yield ( $\phi$ ), as  $B_{CPL} = \epsilon \cdot \phi \cdot |g_{lum}|/2$ .<sup>21</sup>

Chiral lanthanides complexes have been long studied as CPL emitters, displaying large  $|g_{lum}|$  values, sometimes exceeding unity.<sup>22, 23</sup> However, light emission from lanthanide complexes may suffer from modest quantum yields and is severely limited by the absence of any tunability. In order to facilitate the development of CPL-based applications, chiral systems containing organic fluorophores displaying high fluorescence quantum yields and tuneable photophysical properties are recently gaining increasing interest as CPL emitters. Most of the explored CPL emitting organic molecular systems rely on achiral chromophores, chirally perturbed by the introduction of stereogenic motifs such as elements of point, axial, helical or planar chirality.<sup>24-28</sup>

1,4-Diketo-3,6-diarylpyrrolo[3,4-*c*]pyrrole (DPP) derivatives are a class of dyes based on a rigid bilactam core conjugated with two aromatic side groups, known for their intense optical absorption and high fluorescence quantum yields. By varying the nature of the flanking aryl groups it is possible to tune the HOMO-LUMO gap from the green to the near-infrared (NIR) domain.<sup>24, 29, 30</sup> On the other hand, the substituents on the nitrogen position only slightly affect the optical features of isolated DPP dyes, but have a huge impact on the intermolecular interactions, the packing modes and hence the photophysical properties in the solid state.<sup>6, 31</sup> Due to their rigid structures and the extended  $\pi$ -conjugation, the DPP derivatives display aggregation modes often dominated by  $\pi$ -stacking interactions, which eventually lead to the phenomenon known as Aggregation-Caused Quenching (ACQ) consisting in a dramatic reduction of the fluorescence yield upon aggregation. However, sterically demanding groups can reduce the extent of  $\pi$ -stacking interactions, preserving decent emissive properties from the solid state.<sup>6, 32</sup>

Owing to their advantageous photophysical properties, DPP dyes have been studied in few cases as molecular systems for CPL emission: DPP dyes chirally perturbed by enantiopure binaphthyl side groups reached  $|g_{lum}|$  values of  $6 \cdot 10^{-4}$ ,<sup>25</sup> while chiral dyads of DPP units bridged through an enantiopure helicene displayed red CPL emission with a  $|g_{lum}|$  of  $9 \cdot 10^{-4}$  through a mechanism of intramolecular chiral exciton coupling.<sup>24</sup> *N*-alkylation with chiral alkyl chains has

been very recently explored as a synthetic tool for endowing DPP with chiroptical properties either as supramolecular aggregates, whose formation was triggered by hydrogen bonding,<sup>7</sup> or as thin films which were mapped by Mueller Matrix Polarimetry.<sup>16</sup> Moreover, *N*-dihydrocitronellyl chains have been used in a series of DPP-thiophenes, to trigger ECD activity in the solution aggregates. The thiophene rings were functionalized with phenyl, 4-(diphenylamino)phenyl or tetraphenylethylene (TPE) substituents; the former two gave intense ECD spectra of the aggregates in solution, whereas TPE yielded no measurable optical activity.<sup>17</sup> Due to the distance between the stereogenic carbon and the DPP core, isolated molecules remained CD silent in solution in all the derivatives.<sup>17</sup>

In general, all the studies on chiral DPP dyes refer to emissive properties in solution, as for those derivatives ACQ appeared to be dominant in the solid phases. In some cases the ACQ phenomenon can be prevented by using molecular motifs displaying the property of Aggregation Induced Emission (AIE) that is the opposite phenomenon to ACQ. AIE is generally explained as an increased rate of radiative relaxation upon molecular aggregation, due to the blocking of intramolecular motion that would otherwise result in fluorescence quenching. Tetraarylethylenes, siloles, and cyanostilbenes are some of the most well-known motifs displaying AIE properties and they are also, especially TPE, some of the most accessible from a synthetic point of view.<sup>33</sup> Thanks to the practical access to 1,2,2-(triphenyl)ethylenboronic derivatives it is possible to generate various tetraarylethylene functions on other chromophoric scaffolds by Suzuki coupling, provided the presence of reactive aryl halide sites on the substrate. Following this strategy, TPE-DPP derivatives have been synthesized and studied by Tang and coworkers (Fig. 1).<sup>34</sup> However, although containing TPE moieties, most of the *N*-octyl alkylated DPPs reported in this work displayed ACQ behaviour. A partial AIE phenomenon was only observed upon further modification of the molecules by adding phenyl spacers between DPP cores and TPE functions, and by introduction of electron-donating amino groups on the TPE portion of the molecule, which seemed to promote ordered aggregation.<sup>34</sup>

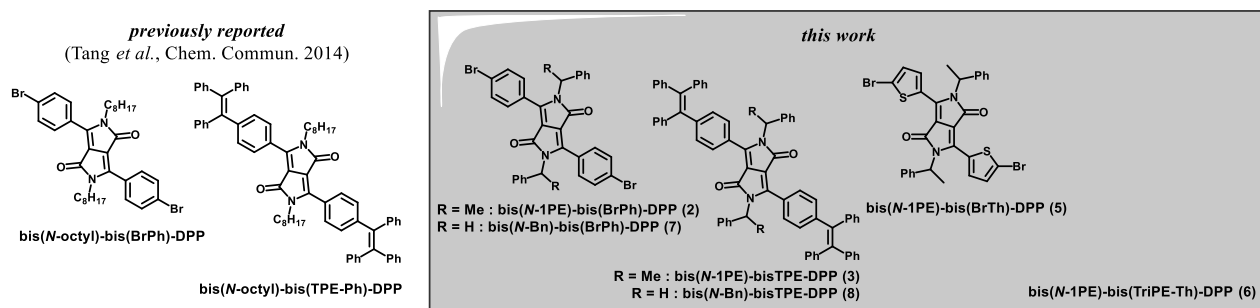


**Fig. 1** Structures of the TPE-DPP derivatives studied in this work, and analogous derivatives previously reported.

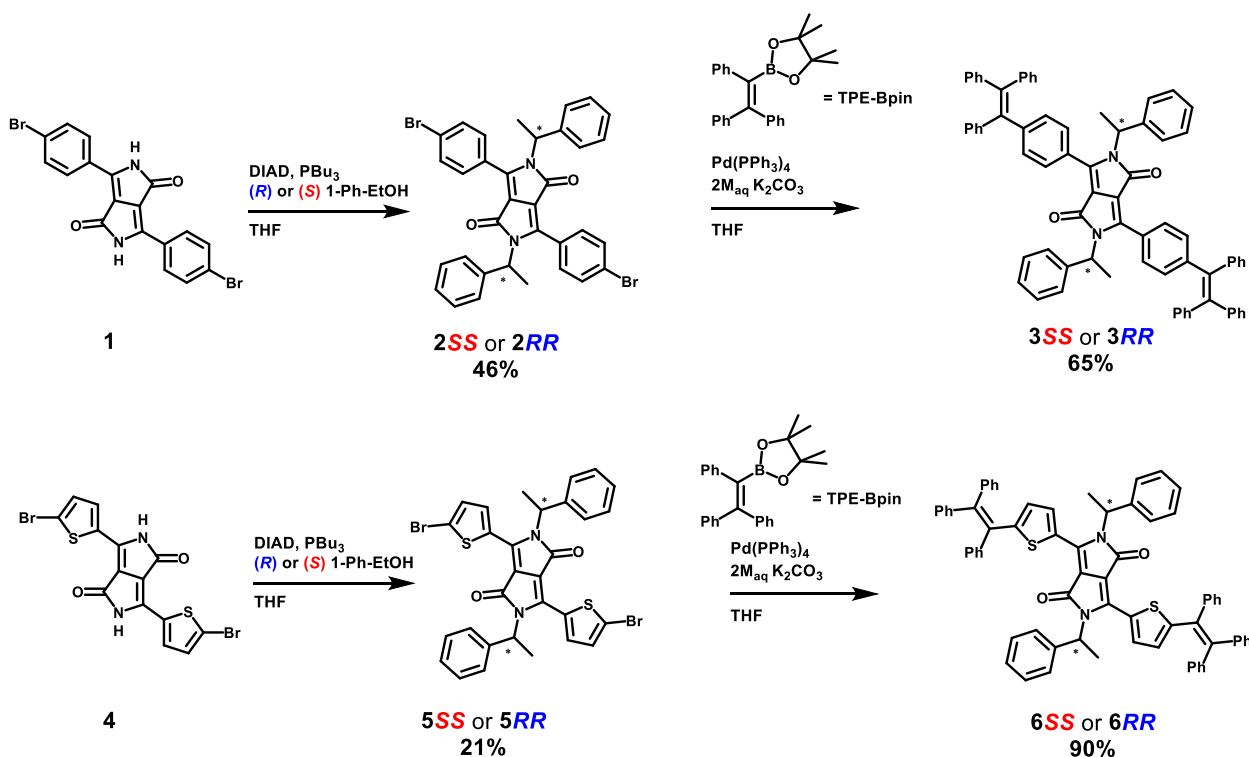
Besides from the enhanced emissive properties of TPE derivatives in aggregates, the use of this structural motif in molecular materials with chiroptical properties is also motivated by the fact that TPE does not lay flat but rather adopts a propeller-shaped conformation, and therefore, upon restriction of molecular motion, the structure can be blocked in one of two possible enantiomeric conformations characterized by enhanced chiroptical responses.<sup>35-37</sup>

In this work, we aimed at obtaining chiral DPP-based materials with enhanced emissive and chiroptical properties from the solid state. To reach such goal, we took advantage of TPE functions applied to a new class of chiral DPP derivatives possessing stereogenic carbons directly connected to the *N*-position (Fig. 1).

## 2. Results and discussion

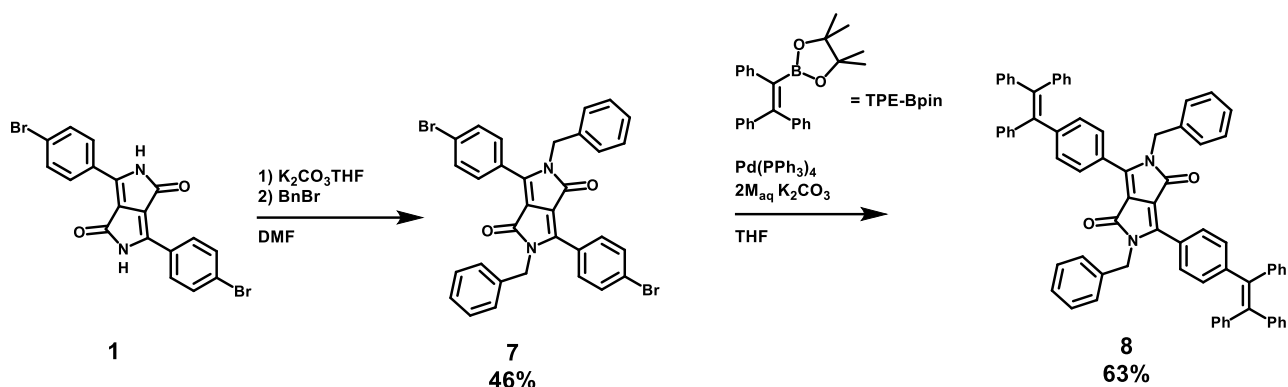
### 2.1 Synthesis and crystal structures of DPP-TPE derivatives

Starting from bis(*p*-bromophenyl)DPP (**1**) that was synthesized according to a previously reported procedure,<sup>34</sup> the two enantiomers of the corresponding bis-(*N*-*sec*-phenethyl)-DPP (**2RR** and **2SS**) were obtained through the newly reported enantioselective protocol based on Mitsunobu reaction with enantiopure 1-phenylethanol reagents.<sup>38</sup> The chiral TPE-DPP derivatives (**3**) were finally obtained by Suzuki-Miyaura coupling between **2** and the pinacol 1,2,2-triphenylethenylboronate (**TPE-Bpin**)<sup>34</sup>. A thienyl analogue of TPE-DPP was also synthesized starting from the commercially available bis(2-bromothiophen-5-yl)DPP (**4**) pigment, that was enantioselectively *N*-functionalized with *sec*-phenethyl groups yielding the soluble **5SS** and **5RR** dyes. As for the synthesis of compounds **3**, the two enantiomers of chiral bis(5-(1,2,2-triphenylvinyl)thiophene-2-yl)DPP **6SS** and **6RR** were obtained by Suzuki-Miyaura coupling with **TPE-Bpin** (Scheme 1 and Fig. S1-S6).



**Scheme 1** Synthetic route to chiral TPE-DPP (**3SS**, **3RR**, **6SS** and **6RR**) derivatives. During the first step, due to the mechanism of the Mitsunobu reaction, a Walden inversion occurs so that starting from the (*R*)-1-phenylethanol or (*S*)-1-phenylethanol, the *SS* and *RR* enantiomers are obtained, respectively, for the compounds **2** and **5**. The second step consist in a Suzuki-Miyaura coupling between the chiral bromo-derivatives of the DPP and the **TPE-Bpin**.

For comparison purposes, the achiral analogue of **3**, namely the bis(*N*-benzyl)-bisTPE-DPP derivative **8**, has been prepared starting from the bis(*p*-bromophenyl)DPP (**1**) upon *N*-benzylation in classical conditions to afford the bis(*N*-benzyl)-bis(*p*-bromophenyl)-DPP **7**,<sup>39</sup> followed by the Suzuki-Miyaura coupling of the latter with **TPE-Bpin** (Scheme 2 and Fig. S7-S8).



**Scheme 2** Synthetic route to the achiral TPE-DPP derivative **8**.

Gratifyingly, single crystals of **3RR** and **8** of suitable size for X-ray diffraction were obtained from liquid-liquid diffusion of methanol into ca.  $10^{-3}$  M solution in chloroform.

The solid-state structure of **3RR** was unambiguously determined by single crystal X-ray diffraction analysis. The compound crystallizes within the non-centrosymmetric space group  $P1$ , with one independent molecule per asymmetric unit (Table 1 and S1-S2). In each molecule, the two TPE moieties adopt complementary conformations which can be defined as  $P$  and  $M$  (Fig. 2 and S9).<sup>37</sup> However owing to a network of intramolecular and intermolecular CH- $\pi$  interactions between asymmetric *sec*-phenethyl groups and TPE moieties, the two TPE are not perfect mirror images to each other.

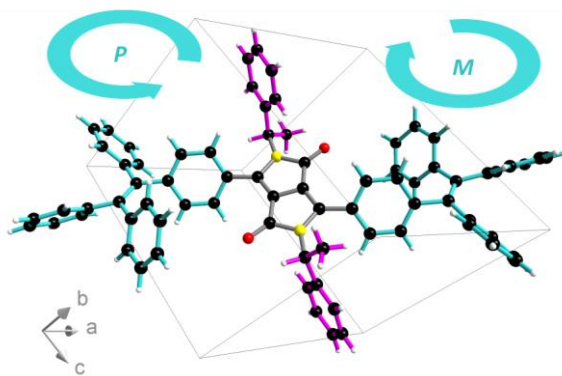


**Fig. 2** Structure of **3RR** in the crystal phase. The arrows highlight the direction of rotation of the propeller, corresponding to a  $P$  conformation for the uphill anticlockwise direction, and  $M$  for the clockwise. The TPE moieties are highlighted in blue and the *sec*-phenethyl groups in pink.

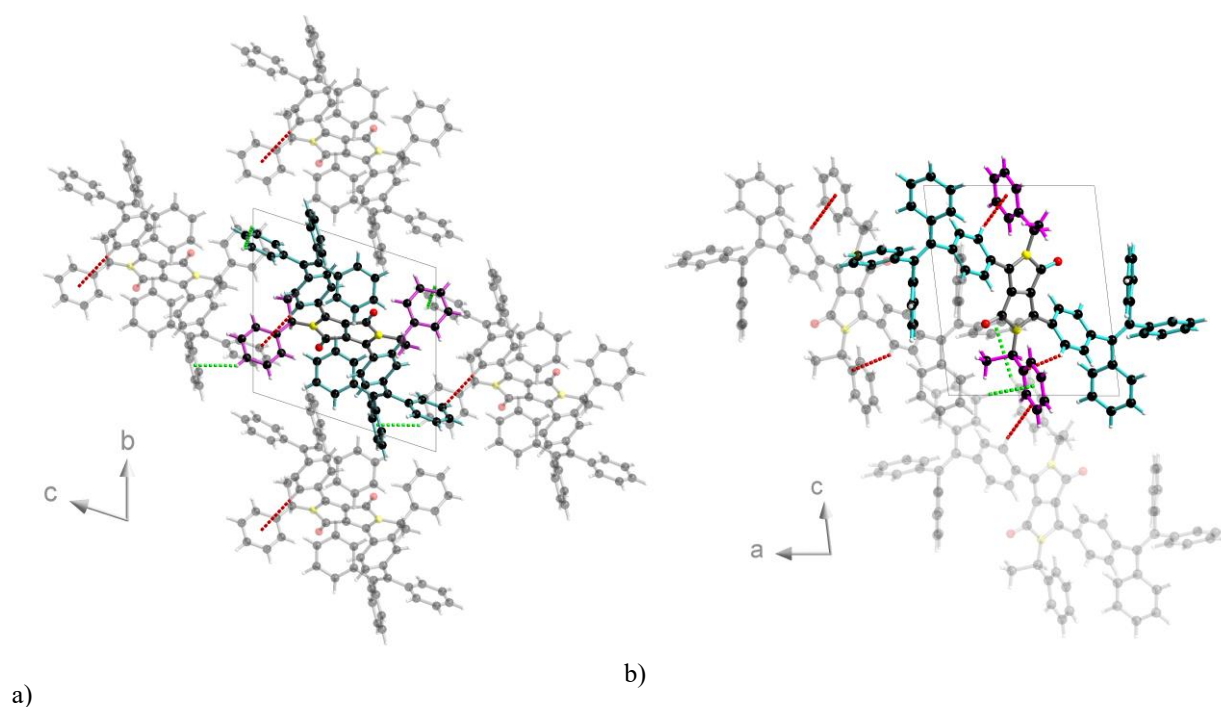


**Fig. 3** Crystal packing of **3RR**, with views along the *a* direction (a), and the *b* direction (b). TPE moieties are highlighted in blue and *sec*-phenethyl (1-PE) groups in pink. Intramolecular (red dotted lines) and intermolecular (green dotted lines) CH- $\pi$  interactions between TPE and 1-PE groups are shown.

In the packing, the DPP cores are well isolated by the bulky TPE and *sec*-phenethyl (1-PE) groups (average distance of 9.622 Å between the closest bilactam units), with the occurrence of CH- $\pi$  intra- and intermolecular interactions (Fig. 3 and S10). Intramolecular TPE-CH to 1-PE  $\pi$  interactions are characterized by distances of 3.066 Å. Intermolecular TPE-CH to 1-PE  $\pi$  interactions have distances of 2.946 Å, while intermolecular 1-PE CH to TPE- $\pi$  interactions display distances of 2.898 Å.

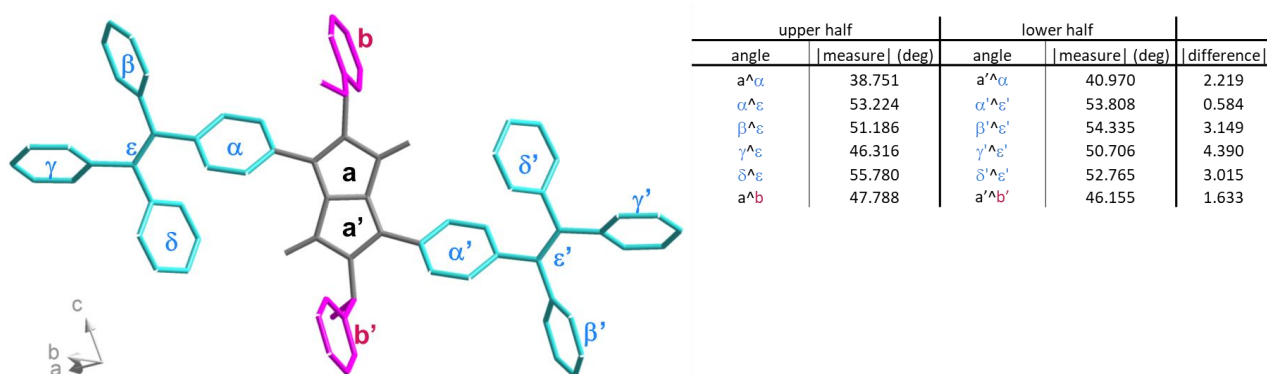


**Fig. 4** Torsional angles between rings within the structure of **3RR** in the crystal phase.

The torsional angles between the central DPP core and the first phenyl rings ( $a^{\wedge}\alpha$  and  $a'^{\wedge}\alpha'$ ) of the TPE moiety, amounting at ca. 40°, have a difference of ca. 2° between each side of the molecule, and even smaller differences, of about half degree between the two halves, are measured for the angles between the first phenyl rings of TPE and the plane containing the



ethylene system ( $\alpha^{\wedge}\varepsilon$  and  $\alpha'^{\wedge}\varepsilon'$ ) (Fig. 4). Bigger differences are detected for the torsional angles between the ethylene system and the remaining phenyl rings of the TPE moiety ( $|\beta^{\wedge}\varepsilon - \beta'^{\wedge}\varepsilon'| = 3.149^\circ$ ,  $|\gamma^{\wedge}\varepsilon - \gamma'^{\wedge}\varepsilon'| = 4.390^\circ$ ,  $|\delta^{\wedge}\varepsilon - \delta'^{\wedge}\varepsilon'| = 3.015^\circ$ ).

On the other hand, compound **8** crystallizes within the centrosymmetric space group  $P-1$ , with half molecule within the asymmetric unit. Therefore, the two TPE units adopt perfect complementary  $M$  and  $P$  conformation within each molecule. Similarly to **3RR**, the TPE moieties help keeping the DPP isolated, as suggested by the average distances of 9.575 Å between the closest bilactam units (Fig. S11-S12, Table S1 and S4-S5).

## 2.2 Photophysical study

The enantiomers of compounds **2** in  $5 \cdot 10^{-5}$  M solutions in chloroform display an unresolved absorption band peaking at 469 nm ( $\varepsilon = 28000 \text{ L} \cdot \text{mol}^{-1} \cdot \text{cm}^{-1}$ ), classically attributed to  $\pi$ - $\pi^*$  transitions in phenyl-flanked DPP derivatives. Replacing the solvent by a chloroform/methanol (1:9) mixture determines a blue shift of 8 nm, without affecting the shape of the peak (Fig. 5a). The ECD spectra show a signal of ca.  $+7.6 \text{ L} \cdot \text{mol}^{-1} \cdot \text{cm}^{-1}$  for the ( $S,S$ ) enantiomer (**2SS**) at the maximum of the main transition, with a perfect mirror image for the ( $R,R$ ) enantiomer (**2RR**), whose amplitude does not evolve upon solvent change (Fig. 6a). Similarly the enantiomers of compound **3** show an unresolved absorption band peaking at 486 nm ( $\varepsilon = 24500 \text{ L} \cdot \text{mol}^{-1} \cdot \text{cm}^{-1}$ ) in chloroform and 475 nm ( $\varepsilon = 18900 \text{ L} \cdot \text{mol}^{-1} \cdot \text{cm}^{-1}$ ) in chloroform/methanol (1:9) mixture (Fig. 5a). This transition is ECD active as well with a signal amplitude of  $+4.6 \text{ L} \cdot \text{mol}^{-1} \cdot \text{cm}^{-1}$  for the ( $S,S$ ) enantiomer (**3SS**), and with a mirror image pattern for the ( $R,R$ ) enantiomer (**3RR**). The absolute value of the intensity of the main ECD band slightly decreases to  $+3.5 \text{ L} \cdot \text{mol}^{-1} \cdot \text{cm}^{-1}$  in chloroform/methanol (1:9) mixture (Fig. 6b).

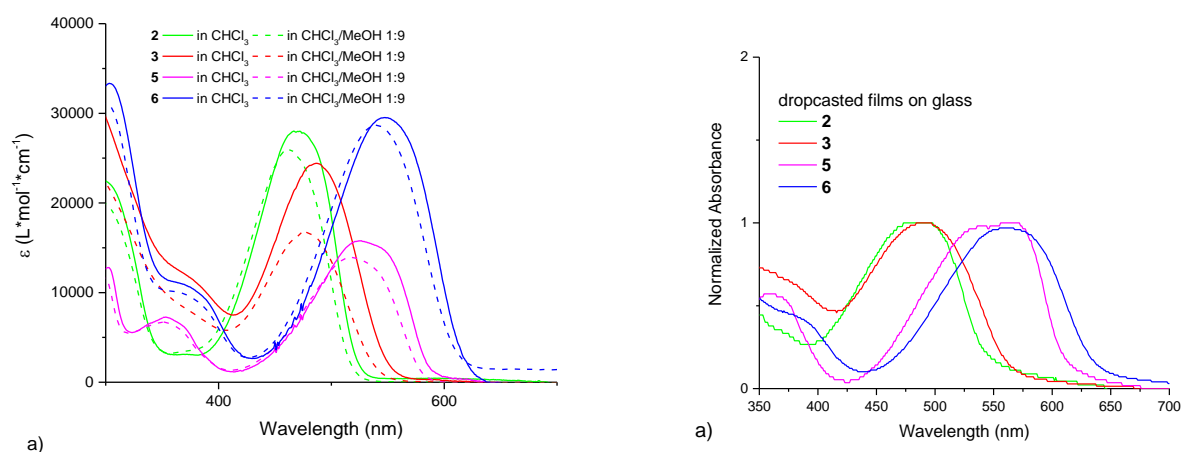


**Fig. 5** Molar extinction coefficient spectra in solution (a), and normalized absorption spectra in the film (b). Absorption spectra in solution are measured at a concentration of  $5 \cdot 10^{-5}$  M in chloroform (continuous line), or in a mixture of chloroform (10% by volume) and methanol. Films are deposited by drop casting from  $10^{-4}$  M solutions in chloroform on glass slides.

Compound **5** in  $10^{-5}$  M solutions in chloroform displays an absorption band peaking at 525 nm ( $\varepsilon = 15700 \text{ L} \cdot \text{mol}^{-1} \cdot \text{cm}^{-1}$ ), that appears slightly structured as in other thienyl-DPP derivatives, but not resolved. Replacing the solvent by a chloroform/methanol (1:9) mixture determines a blue shift of 6 nm, and a slight hypochromism with a decrease of  $\varepsilon$  to  $14000 \text{ L} \cdot \text{mol}^{-1} \cdot \text{cm}^{-1}$  (Fig.



5a). The ECD spectroscopy shows a signal of ca.  $+3.7 \text{ L} \cdot \text{mol}^{-1} \cdot \text{cm}^{-1}$  for the (*S,S*) enantiomer (**5SS**) at the maximum of the main transition, with a perfect mirror image for the (*R,R*) enantiomer (**5RR**), that does not evolve in chloroform/methanol (1:9) mixture (Fig. 6c). Similarly the enantiomers of compound **6** show an absorption band peaking at 548 nm ( $\epsilon = 29500 \text{ L} \cdot \text{mol}^{-1} \cdot \text{cm}^{-1}$ ) in chloroform and 538 nm in chloroform/methanol (1:9) mixture with a slight hypochromism ( $\epsilon = 28700 \text{ L} \cdot \text{mol}^{-1} \cdot \text{cm}^{-1}$ ) (Fig. 5a). This transition is ECD active as well, with a signal amplitude of  $+7.6 \text{ L} \cdot \text{mol}^{-1} \cdot \text{cm}^{-1}$  for the (*S,S*) enantiomer (**6SS**) and a mirror image pattern for the (*R,R*) enantiomer (**6RR**). The absolute value of the ECD intensity decreases to  $+6.4 \text{ L} \cdot \text{mol}^{-1} \cdot \text{cm}^{-1}$  in chloroform/methanol (1:9) mixture (Fig. 6d).

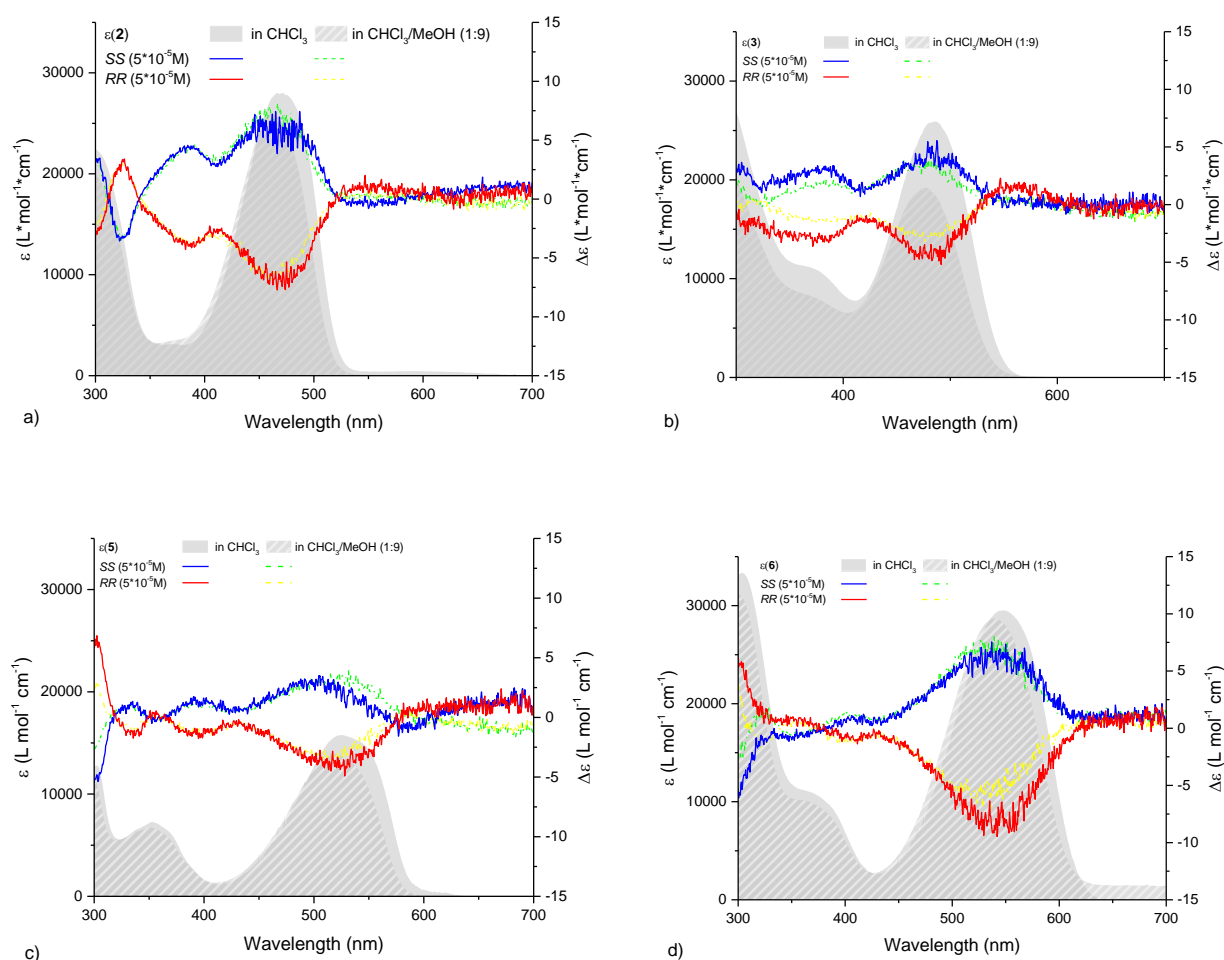


**Fig. 6** ECD spectra for each couple of enantiomers (*SS* in blue and green, *RR* in red and yellow) in  $10^{-5}$  M solutions in chloroform (continuous blue and red lines) or chloroform 10% (v/v) in methanol (dashed green and yellow lines), for compounds **2** (a), **3** (b), **5** (c), and **6** (d). In grey shade, the corresponding molar extinction coefficient spectra.

In the film, the absorption spectra of compounds **2** and **3** broaden and the main peaks are 18 nm and 9 nm red-shifted, respectively. Films of **5** and **6** display a broadened absorption, with 37 nm and 16 nm red shift, respectively, compared to chloroform solutions. The compound **5** exhibits a remarkable red-shift in the solid phase compared to solution. This can be explained as an increased contribution of the low energy shoulder (Fig. 5b), which can be attributed to an increased contribution from J aggregates.<sup>40</sup>

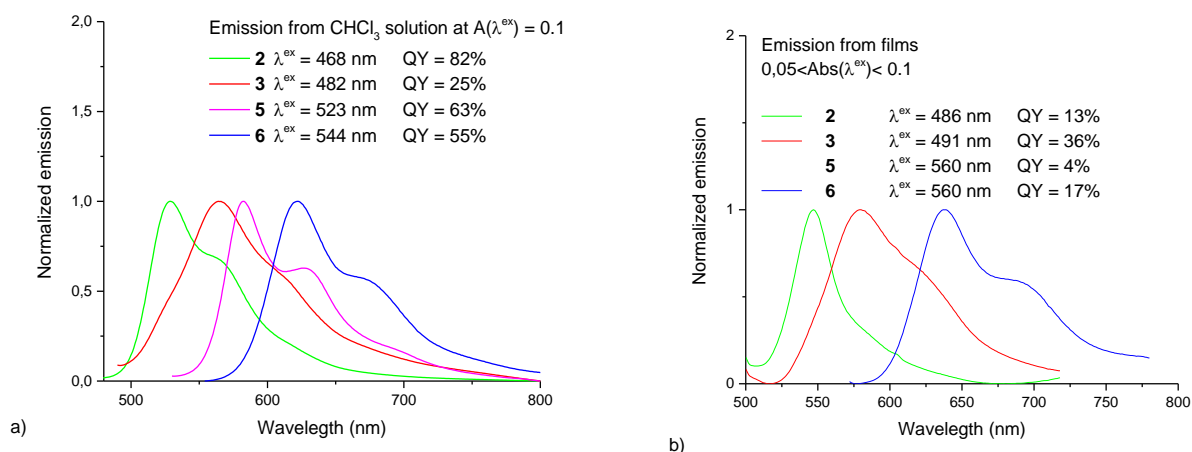


**Fig. 7** Photoluminescence spectra from chloroform solutions (a) and films (b). Solutions have a concentration that correspond to an absorbance of 0.1 in a 10 mm cell, at the excitation wavelength noted in the legend. Similarly, films have an absorbance comprised between 0.05 and 0.1. Fluorescence spectrum from compound 5 is not showed. Quantum yields are measured using an integrating sphere, in CHCl<sub>3</sub> solutions and on powders at absorptances comprised between 0.05 and 0.15.

Compound 2 in  $3 \cdot 10^{-5}$  M chloroform solutions, under excitation at 468 nm, shows emission peaking at 548 nm, with a shoulder at 562 nm, with a quantum yield of 82% (

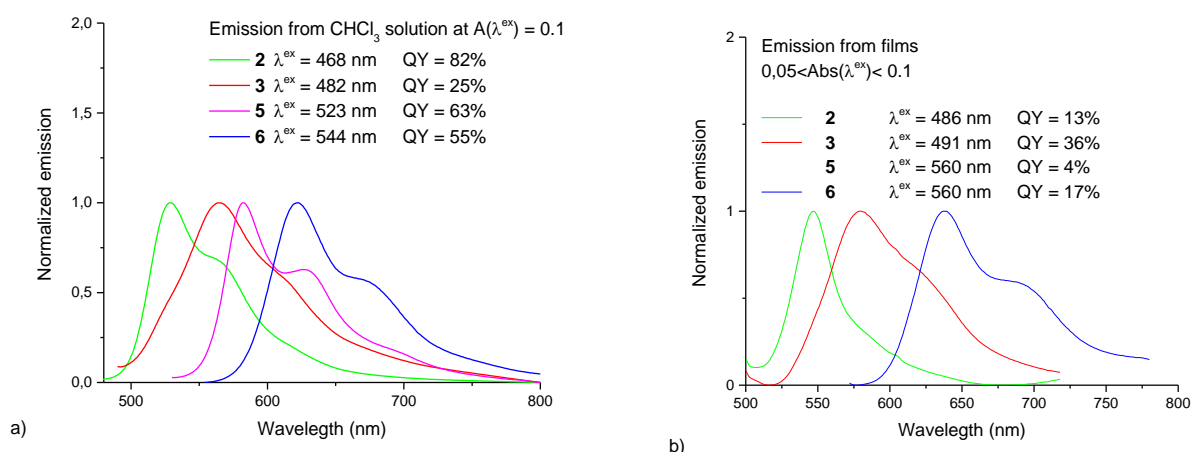


**Fig. 7a).** Compound 3 in  $4 \cdot 10^{-5}$  M chloroform solutions emits light at 564 nm, with a shoulder at 606 nm, with a quantum yield of 25% (

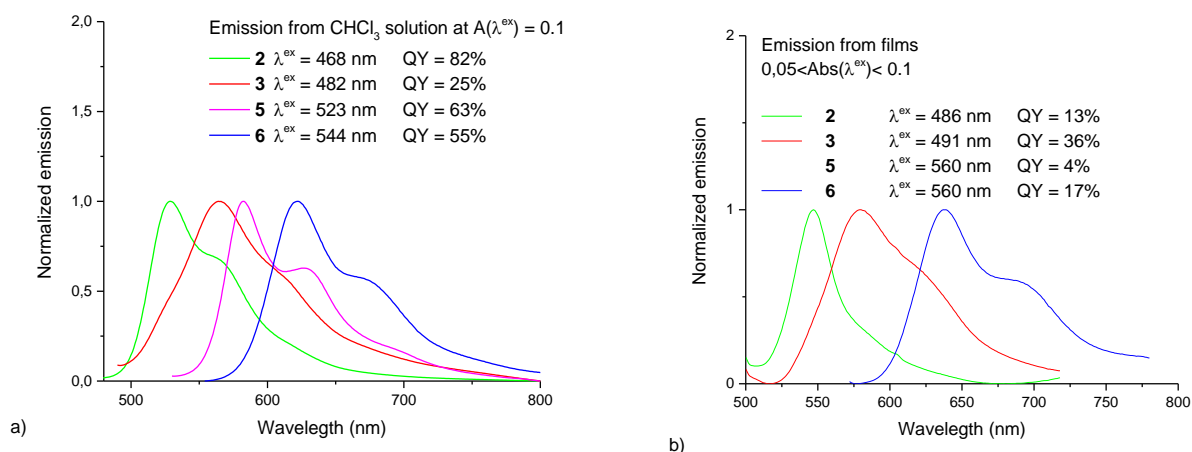


Fig. 7a). Compound **5** in  $6 \cdot 10^{-5}$  M chloroform solution emits light with a vibronic progression peaking at 582 nm, 628 nm and 692 nm, with a quantum yield of 63% (

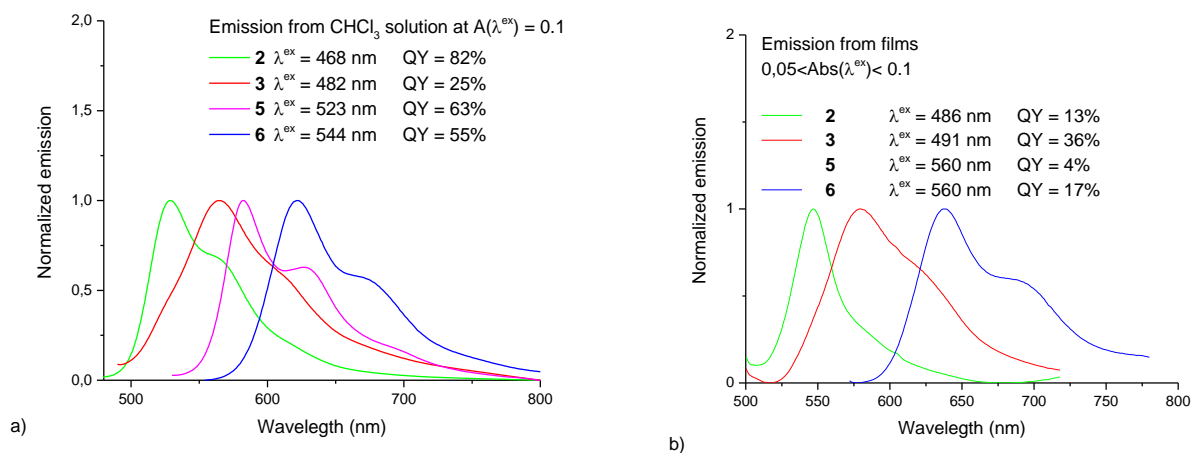


Fig. 7a). Compound **6** in  $3 \cdot 10^{-5}$  M chloroform solution emits light at 622 nm, with a shoulder at 672 nm, with a quantum yield of 55% (

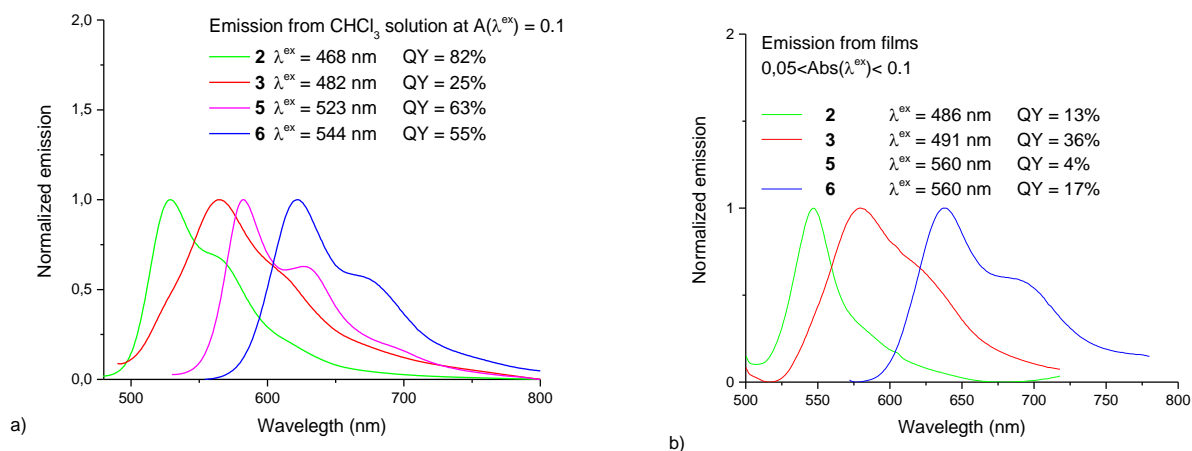


Fig. 7a). In solid samples: the compound **2** emits within an unresolved band peaking at 547 nm with a quantum yield of 13%. Compound **3** shows an emission band peaking at 579 nm, with a

shoulder at ca. 621 nm and a quantum yield of 36%. Compound **5** emits very weak photoluminescence, whose profile is not shown in

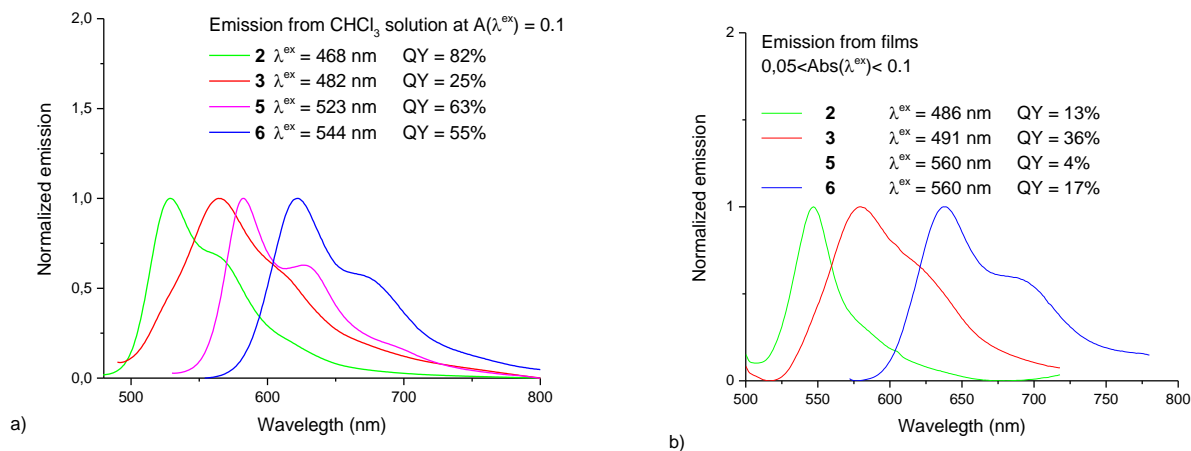


Fig. 7b as it is dominated by noise, corresponding to a quantum yield not exceeding 4%. Compound **6** emits an almost resolved vibronic progression starting at 637 nm, with a second peak at 689 nm, and a quantum yield of 17%. Finally, compound **8** emits fluorescence at 594 nm, with a shoulder at 621 nm, and a quantum yield of 27%.

In summary, compounds **2** and **5** are affected by ACQ as expected, even if residual fluorescence is still detectable from compound **2** in the solid state. Conversely, compounds **3** and **6** are not completely quenched in solution, thus they cannot be considered as AIE-gens. However, the compound **3** displays an enhanced fluorescence in the solid compared to the solution, therefore it is possible to claim an aggregation-enhanced emission (AEE) for this compound. Indeed, the difference between AIE and AEE phenomena resides in the fact that in the former case the fluorophore is (almost) totally quenched in solution, while in the latter the fluorescence quenching is only partial. On the other hand, compound **6** displays a classic ACQ behaviour despite the presence of a tetraarylethylene system. This can be ascribed to the lower steric demand of thiophene rings, compared to phenyls, which can accommodate into a more planar structure prone to  $\pi$ -stacking interactions.

All the compounds display detectable ECD signals all over the UV-vis absorption region, indicating that introduction of chiral *N*-substituents provide significant perturbation to the extended chromophores. However, in any case, the signals do not seem to evolve upon aggregation. Under the hypothesis that in the solid compounds adopt fewer and more precise preferential conformations, thus enhancing ECD features, measurements on dropcasted films and powders dispersed into KBr pellets were performed. Unfortunately all the measurements were not conclusive as heavily affected by artefacts.

### 2.3 Theoretical study

To further investigate the electronic and optical properties of the TPE-DPP derivatives, the electronic structures of the most stable conformations of compounds **2RR** (Fig. S13-S20), **2SS** (Fig. S21-S28), **3RR** (Fig. S29-S32), **3SS** (Fig. S33-S36) and **8** (Fig. S37-S41), in the gas phase, were calculated using a Density Functional Theory (DFT) approach for the ground state and a Time Dependent DFT method for the optical properties. For both the hybrid functional PBE0<sup>41</sup> and the TZVP<sup>42</sup> basis set have been used with the Gaussian 09 program.<sup>43</sup> The ground states have been verified as minima on the potential energy surface with a frequency calculation. The Molecular orbital and electron density differences isosurfaces were calculated and represented with a homemade python program<sup>44</sup> based on cclib.<sup>45</sup> The energy gaps between HOMO and

LUMO of compounds **2**, **3**, and **8** are 3.1 eV, 2.95 eV, and 2.82 eV respectively, and correspond to transitions with  $\pi$ - $\pi^*$  character mostly located on the DPP core.

The simulated absorption spectrum of the achiral compound **8** shows four relevant absorption bands, the first at 521 nm ( $\pi$ - $\pi^*$  mainly located on the DPP core), the second at 410 nm ( $\pi$ - $\pi^*$  mainly located on the DPP core with participation of the ethylene moieties of TPE), the third at 346 nm ( $\pi$ - $\pi^*$  extended on the whole conjugated system), and the fourth at 320 nm ( $\pi$ - $\pi^*$  mainly located on the TPE moieties), as shown in Fig. S40. Compared to the experimental spectrum (Fig. S42, black line) the lowest energy simulated transition appears overestimated by around 23 nm, while the transitions at 410 nm and 346 nm can be associated to the large bump around 374 nm in the experimental spectrum.

The simulated spectrum of compounds **2** shows two relevant absorption bands, the first at 462 nm ( $\pi$ - $\pi^*$ ) and the second at 310 nm ( $n$ - $\pi^*$ ), shown in Fig. S19a and S27a, in good agreement with the experiment. The rotational strengths, that are calculated as  $+1.9 \cdot 10^{-40}$  esu<sup>2</sup> cm<sup>2</sup> at 462 nm and  $-80.7 \cdot 10^{-40}$  esu<sup>2</sup> cm<sup>2</sup> at 310 nm for the **RR** enantiomer, are not accurately reproduced in the ECD spectra, suggesting the presence of many conformations contributing to the experimental spectra.

On the other hand, the simulated spectra of **RR** and **SS** enantiomers of compound **3** show four relevant absorption bands, the first at 502 nm ( $\pi$ - $\pi^*$ , Fig. 8a), the second at 402 nm ( $\pi$ - $\pi^*$  with larger involvement of the TPE moieties, Fig. 8b), the third including two lines at 345 nm and 343 nm (with  $n$ - $\pi^*$  character partially involving the oxygen non-bonding electron pairs and the *N*-sec-phenethyl group, Fig. 8c and Fig. 8d), and a fourth at 321 nm (mainly located on the TPE moiety, Fig. 8e). Compared to the experimental spectrum the lowest energy transition appears overestimated by around 16 nm, while the cluster of transitions between 402 nm and 343 nm can be associated to a large bump around 374 nm in the experimental spectrum. The rotational strengths are calculated as  $-16.4 \cdot 10^{-40}$  esu<sup>2</sup> cm<sup>2</sup> at 502 nm,  $-11.7 \cdot 10^{-40}$  esu<sup>2</sup> cm<sup>2</sup> at 402 nm,  $-4.5 \cdot 10^{-40}$  esu<sup>2</sup> cm<sup>2</sup> at 345 nm,  $-8.4 \cdot 10^{-40}$  esu<sup>2</sup> cm<sup>2</sup> at 343 nm and  $6.5 \cdot 10^{-40}$  esu<sup>2</sup> cm<sup>2</sup> at 321 nm for the **RR** enantiomer, that are consistent with the fact that the sign of experimental ECD bands remains negative over a wide wavelength range.

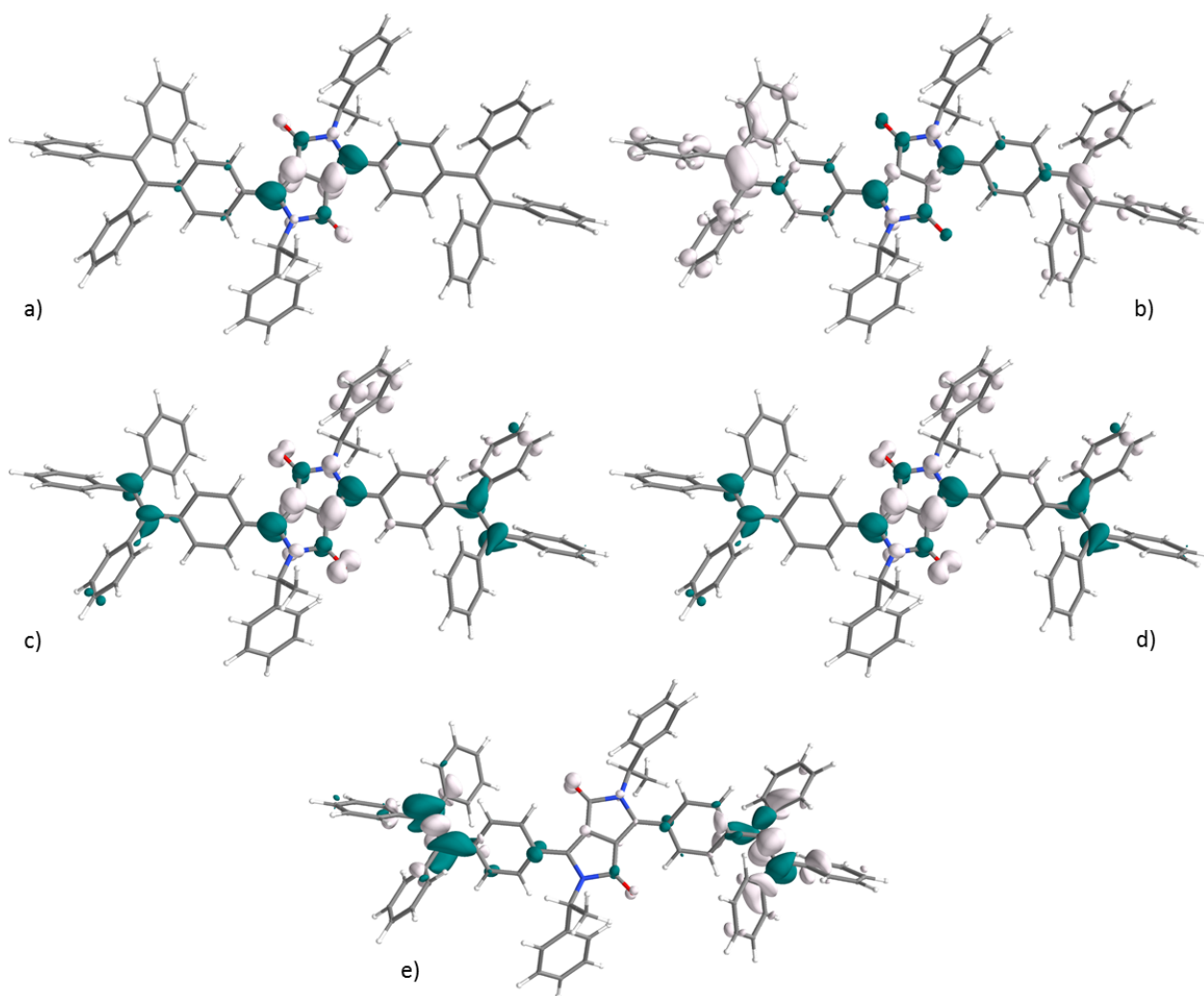


**Fig. 8** Representation of the Electron Density Difference (EDD) associated to the strongest transitions calculated for the compound **3RR**: a) S0-S1; b) S0-S3; c) S0-S6; d) S0-S7; e) S0-S8; excited electrons and holes indicated by green and white surfaces, respectively.

#### 2.4 AEE and CPL emission study

The photoluminescence behaviour of compounds **3** and **8** were further studied in aggregate states in a series of THF/water mixtures (Fig. 9). Compound **3** shows a 2-fold enhancement of the fluorescence intensity when the water fraction increases from 0% to 70%, accompanied by an increase of the quantum yield from 17% up to 28%. At higher water fraction values, up to 90% of water, intensity and quantum yield decrease slightly. On the other hand, compound **8** shows a 3.5-fold enhancement of the fluorescence intensity when the water fraction increases from 0% to 50%, accompanied by an increase of the quantum yield from 20% up to 58%. Once again, a further increase in water content makes fluorescence intensity and quantum yield gradually drop (Fig. 9). This behaviour has also been reported in a recent work on chiral fluorophores displaying AEE properties, and attributed to the formation of a precipitate.<sup>46</sup>

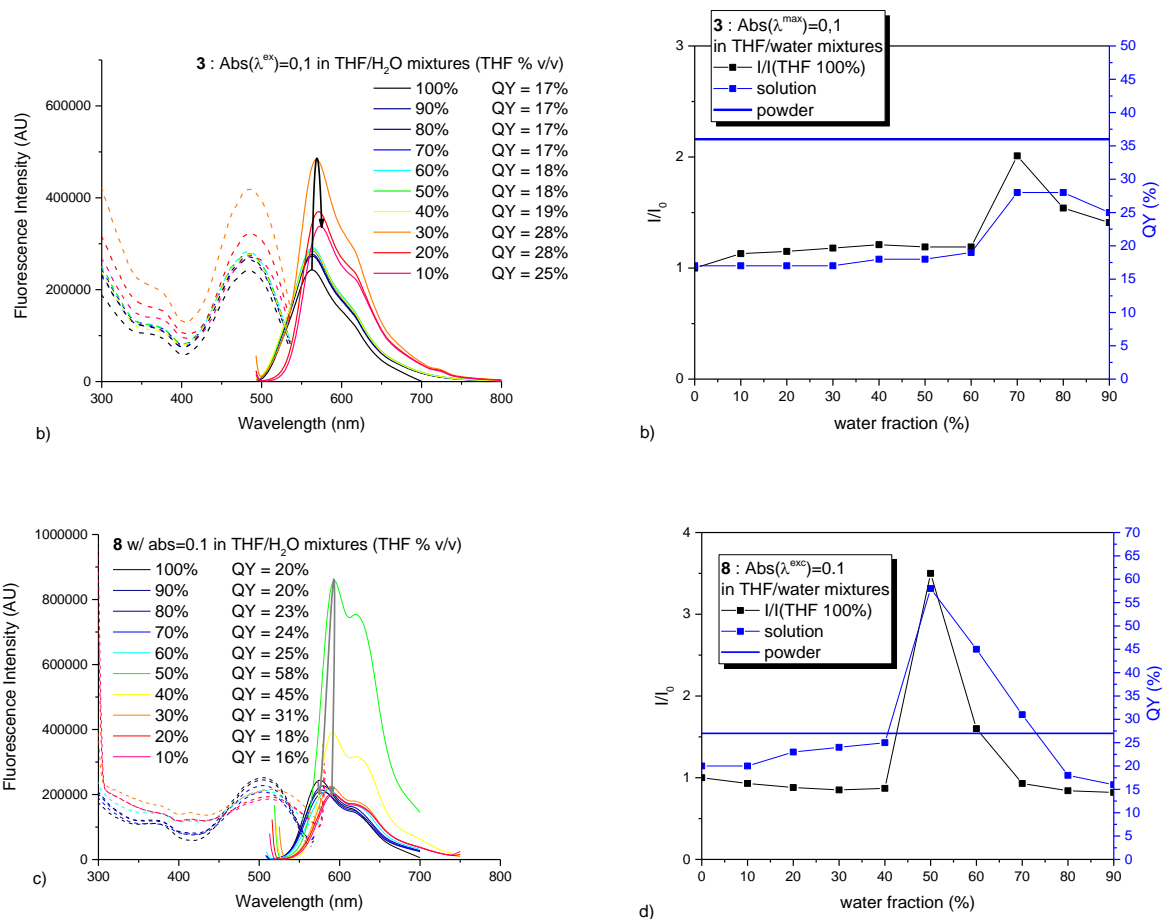


**Fig. 9** Emission and excitation spectra of compounds **3** and **8** in THF/water mixtures, displaying the corresponding values of fluorescence quantum yield and  $I/I_0$  ratio. In details: a) emission (solid lines) and excitation (dashed lines) spectra of **3** in a series of THF/water mixtures, from 100% THF (black lines) to 10% THF (red lines), with respective quantum yield (QY) values; b) diagram of quantum yield and  $I/I_0$  ratio for **3**, as a function of the water fraction, being  $I_0$  the intensity of the emission peak in pure THF; c) emission (solid lines) and excitation (dashed lines) spectra of **8** in a series of THF/water mixtures, from 100% THF (black lines) to 10% THF (red lines), with respective quantum yield (QY) values; d) diagram of quantum yield and  $I/I_0$  ratio for **8**, as a function of the water fraction, being  $I_0$  the intensity of the emission peak in pure THF.

Compound **3** dissolved at concentration of  $10^{-6}$ M in  $\text{CHCl}_3$ , emitted detectable CPL under excitation at 365 nm, with  $|g_{lum}|$  around  $2 \cdot 10^{-4}$ , with positive values for the *SS* enantiomer, and negative for *RR* (Fig. S43). The sign and magnitude of  $g_{lum}$  is coherent with the absorption dissymmetry factor associated to the most red shifted Cotton effect in the ECD spectrum. The  $B_{CPL}$  value was estimated approximately  $0.6 \text{ M}^{-1}\text{cm}^{-1}$ .<sup>21</sup>

### 3. Conclusion

In summary, four pairs of enantiomers of organic fluorescent tetraarylethylene-DPP derivatives (*RR* and *SS* enantiomers of compounds **2**, **3**, **5**, and **6**), bearing  $\alpha$ -chiral *N*-substituents have been synthesized and characterised. Single-crystals X-ray diffraction experiments revealed that compound **3** adopt complementary *M* and *P* conformation for the two TPE moieties, although not as perfect mirror images. The DFT calculation confirmed that despite the complementary *M* and *P* conformation, a non-negligible rotational strength is associated to all the electronic transitions. All of them displayed ECD activity extended to all the UV-vis absorption features. Further studies on fluorescent emission of compound **3**, and its achiral homologue **8**, in THF/water mixture showed that both have AEE properties, exhibiting higher fluorescent quantum yields in aggregate states formed as the water fraction increases. These results are consistent with the fact that they are remarkably fluorescent in solid state.



To this point it is important to highlight the role of benzyl-type *N*-substituents, that thanks to their steric demand help in preventing  $\pi$ - $\pi$  stacking interactions and ACQ. Indeed, while previously reported analogous TPE-DPP derivatives *N*-alkylated with linear alkyl chains displayed fluorescence quantum yields of 11% in the solid state, compound **8** and **3** (*N*-alkylated with increasing sterically demanding benzyl and *sec*-phenethyl groups, respectively) reached quantum yield values of 27% and 36%, respectively.

These results suggest an interesting direction towards the development of DPP-based fluorophores with enhanced emission from aggregate states, capable of emitting circularly polarized light with possibility of increasing  $g_{lum}$  factors upon control of the aggregation mode. The combination of chiroptical activity with the aggregation-induced phenomena is indeed expected to attract great interest in the development of new fluorescent probes for imaging,<sup>47-49</sup> that would thus result amenable to be stimulated and/or read under circularly polarised light with potential enhancement of the signal-to-noise ratio.

## 4. Experimental

### 4.1 Materials and methods

All commercially available reagents and solvents were used as received unless otherwise noted. Dry tetrahydrofuran was directly used from the purification machines. Chloroform as solvent for synthesis was distilled over calcium hydride prior to use. Chromatography purifications were performed on silica gel Sorbent Technologies Silica Gel (60 Å, 65 x 250 mesh) and thin layer chromatography (TLC) was carried out using aluminum sheets precoated with silica gel 60 (EMD 40–60 mm, 230–400 mesh with 254 nm dye). All reactions were carried out in Schlenk tubes under argon atmosphere. Dropwise additions were done with a programmable syringe pump. NMR spectra were acquired on a Bruker Avance DRX 300 and 500 spectrometers operating at 300 and 500 MHz for <sup>1</sup>H and 75 and 125 MHz for <sup>13</sup>C, respectively, at room temperature in CDCl<sub>3</sub> solutions. <sup>1</sup>H and <sup>13</sup>C NMR spectra were referenced to the residual protonated solvent (<sup>1</sup>H) or the solvent itself (<sup>13</sup>C). All chemical shifts are expressed in parts per million (ppm) downfield from external tetramethylsilane (TMS), using the solvent residual signal as an internal standard and the coupling constant values (J) are reported in Hertz (Hz). The following abbreviations have been used: s, singlet; dd, doublet of doublets; m, multiplet. Mass spectrometry MALDI-TOF MS spectra were recorded on Bruker Biflex - IITM apparatus, equipped with a 337 - nm N<sub>2</sub> laser

The spectroscopic properties of the derivatives **2**, **3**, **5** and **6** were evaluated in solutions at concentrations of 5\*10<sup>-5</sup> M for absorption measurements on Shimadzu UV-1800 spectrometer, and at adjusted concentrations corresponding to an absorbance of 0.1 for fluorescence measurements on RF-6000 fluorimeter. The absorption spectroscopy and circular dichroism spectroscopy of **2**, **3**, **5** and **6** as isolated molecules were recorded in chloroform solutions on a JASCO J-1500 spectrometer at 20 °C, while in order to assess the effect of aggregation a mixture of chloroform/methanol (1:9) was used as solvent, by keeping the solute concentration at 5\*10<sup>-5</sup>M.

Spectrophotometry and fluorimetry in the solid state were recorded on films of **2**, **3**, **5** and **6** drop-casted from 10<sup>-4</sup> solutions in CHCl<sub>3</sub> onto glass slides. Fluorescence quantum yields were measured on JASCO FP-8500 fluorimeter equipped with an integrating sphere, in 5\*10<sup>-5</sup> chloroform solutions and in solid powder spread between glass slides, with absorptance comprised between 0.05 and 0.15 (average on 4 measures). CPL spectra of **3RR/3SS** were recorded in 10<sup>-6</sup> M CHCl<sub>3</sub> solution with a home-built instrument under 365 nm irradiation by using a 90° geometry between excitation and detection.<sup>50</sup>

## 4.2 Synthesis

### Synthesis of 2,5-bis((S)-1-phenylethyl)-3,6-bis(4-(1,2,2-triphenylvinyl)phenyl)-2,5-dihydropyrrolo[3,4-c]pyrrole-1,4-dione (**3SS**)

In a Schlenk tube, **2SS**<sup>38</sup> (50 mg, 0.076 mmol, 1eq.), TPE-Bpin<sup>34</sup> (64 mg, 0.168 mmol, 2.2 eq.), and Pd(PPh<sub>3</sub>)<sub>4</sub> (2.7 mg, 0.0023 mmol, 0.03 eq.) were charged and purged with three vacuum/argon cycles. THF (2.5 mL) and aqueous K<sub>2</sub>CO<sub>3</sub> (2 M, 0.8 mL, 20 eq.) previously degassed, were injected into the reaction vessel, and the resulting mixture was stirred at reflux overnight. Once the reaction completed, the crude was extracted into dichloromethane, and washed with water. The organic layer was dried over anhydrous MgSO<sub>4</sub>, and the solvent removed under reduced pressure. The crude was purified by silica gel column chromatography with a mixture of petroleum ether / dichloromethane (3:2) as the eluent, affording 49 mg (64% yield) of **3SS** as a bright orange powder.

Similarly, **3RR** was obtained from **2RR** following the same procedure.

<sup>1</sup>H NMR (300 MHz, CDCl<sub>3</sub>) δ = 7.33 – 7.19 (m, 16H), 7.15 – 6.99 (m, 32H), 5.29 (q, J = 6.9 Hz, 2H), 1.77 (d, J = 7.1 Hz, 6H) ppm.

<sup>13</sup>C NMR (76 MHz, CDCl<sub>3</sub>) δ = 163.01, 149.06, 146.80, 143.58, 143.39, 142.96, 142.59, 141.60, 141.53, 140.35, 131.71, 131.52, 131.39, 128.57, 127.99, 127.95, 127.81, 127.27, 126.96, 126.85, 126.27, 110.49, 53.22, 18.42 ppm.

HRMS (DCTB, M+) calcd for C<sub>74</sub>H<sub>56</sub>N<sub>2</sub>O<sub>2</sub><sup>+</sup> 1004.43368; found 1004.43363.

### Synthesis of 3,6-bis(5-bromothiophen-2-yl)-2,5-bis((S)-1-phenylethyl)-2,5-dihydropyrrolo[3,4-c]pyrrole-1,4-dione (**5RR**)

Under argon atmosphere, tributylphosphine (1.08 mL, 4.37 mmol, 5eq.) was dissolved in dry THF (3 mL) and the mixture cooled at 0°C, then DIAD (1.03 mL, 4.37 mmol, 5eq.) was added dropwise, resulting in a rapid loss of DIAD's bright yellow tint upon formation of a complex with the phosphine. In a separate Schlenk tube, under argon atmosphere, **4** (400 mg, 0.87 mmol, 1eq.) was dispersed in dry THF (10 mL) and the mixture cooled at 0°C. The mixture containing the Bu<sub>3</sub>P/DIAD complex was added dropwise into the second Schlenk tube resulting in a bluish purple solution. At this point, (*R*)-1-phenylethanol (0.53 mL, 4.37 mmol, 5 eq.) dissolved in THF (1 mL) was injected dropwise to the mixture over 5h. The mixture was then allowed to reach rt and kept under stirring overnight.

The mixture was poured in 1M aqueous HCl and extracted into dichloromethane. The organic layer was first washed with water, then dried over anhydrous MgSO<sub>4</sub> and the solvent removed under reduced pressure. The crude was purified by silica gel column chromatography with a mixture of petroleum ether / dichloromethane (2:3) as the eluent, affording 120 mg (21% yield) of **5RR** as a dark reddish powder.

Similarly, **5SS** was obtained from (*S*)-1-phenylethanol following the same procedure.

<sup>1</sup>H NMR (300 MHz, CDCl<sub>3</sub>) δ = 7.88 (d, J = 4.1 Hz, 2H), 7.38 – 7.27 (m, 10H), 7.10 (d, J = 4.1 Hz, 2H), 5.73 (q, J = 7.2 Hz, 2H), 1.96 (d, J = 7.1 Hz, 6H) ppm.

<sup>13</sup>C NMR (76 MHz, CDCl<sub>3</sub>) δ = 161.74, 140.68, 140.16, 134.44, 131.42, 130.58, 128.81, 127.55, 126.51, 119.29, 109.84, 53.58, 18.39 ppm.

HRMS (DCTB, M+) calcd for C<sub>30</sub>H<sub>22</sub>N<sub>2</sub>O<sub>2</sub>S<sub>2</sub>Br<sub>2</sub><sup>+</sup> 663.94910; found 663.94840.

### Synthesis of 2,5-bis((S)-1-phenylethyl)-3,6-bis(5-(1,2,2-triphenylvinyl)thiophen-2-yl)-2,5-dihydropyrrolo[3,4-c]pyrrole-1,4-dione (**6RR**)

**5RR** (80 mg, 0.120 mmol, 1eq.), TPE-Bpin<sup>34</sup> (101 mg, 0.264 mmol, 2.2 eq.), and Pd(PPh<sub>3</sub>)<sub>4</sub> (4.2 mg, 0.0036 mmol, 0.03 eq.) were charged in a Schlenk tube and purged with three

vacuum/argon cycles. THF (2.5 mL) and aqueous K<sub>2</sub>CO<sub>3</sub> (2 M, 1.2 mL, 20 eq.) previously degassed, were injected into the reaction vessel, and the resulting mixture was stirred at reflux overnight. Once the reaction completed, the crude was extracted into dichloromethane, and washed with water. The organic layer was dried over anhydrous MgSO<sub>4</sub>, and the solvent removed under reduced pressure. The crude was purified by silica gel column chromatography with a mixture of petroleum ether / dichloromethane (2:3) as the eluent, affording 100 mg (90% yield) of **6RR** as a purple powder.

Similarly, **6SS** was obtained from **6SS** following the same procedure.

<sup>1</sup>H NMR (499 MHz, CDCl<sub>3</sub>) δ = 8.06 (d, J = 4.0 Hz, 2H), 7.41 – 7.31 (m, 8H), 7.30 – 7.19 (m, 10H), 7.10 – 7.06 (m, 6H), 7.04 (d, J = 4.0 Hz, 2H), 7.03 – 7.00 (m, 4H), 6.98 – 6.92 (m, 6H), 6.89 – 6.85 (m, 4H), 6.68 (s, 2H), 5.61 (q, J = 6.8 Hz, 2H), 1.82 (d, J = 7.1 Hz, 6H).

<sup>13</sup>C NMR (125 MHz, CDCl<sub>3</sub>) δ = 161.90, 149.05, 144.18, 141.79, 140.92, 140.76, 139.65, 137.17, 134.74, 132.61, 131.85, 131.29, 130.80, 130.13, 129.31, 129.00, 128.71, 128.49, 128.45, 128.19, 127.90, 127.86, 127.12, 127.05, 126.57, 109.40, 53.64, 18.11 ppm.

HRMS (DCTB, M+) calcd for C<sub>70</sub>H<sub>52</sub>N<sub>2</sub>O<sub>2</sub>S<sub>2</sub><sup>+</sup> 1016.34529; found 1016.34647.

### Synthesis of 2-benzyl-5-(1-phenylethyl)-3,6-bis(4-(1,2,2-triphenylvinyl)phenyl)-2,5-dihydropyrrolo[3,4-c]pyrrole-1,4-dione (**8**)

**7** (50 mg, 0.80 mmol, 1 eq.),<sup>39</sup> TPE-Bpin (67 mg, 0.175 mmol, 2.2 eq.),<sup>34</sup> and Pd(PPh<sub>3</sub>)<sub>4</sub> (5.5 mg, 0.0048 mmol, 0.06 eq.) were charged in a Schlenk tube and purged with three vacuum/argon cycles. THF (2.5 mL) and aqueous K<sub>2</sub>CO<sub>3</sub> (2 M, 0.8 mL, 20 eq.) previously degassed, were injected into the reaction vessel, and the resulting mixture was stirred at reflux overnight. Once the reaction completed, the crude was extracted into dichloromethane, and washed with water. The organic layer was dried over anhydrous MgSO<sub>4</sub>, and the solvent removed under reduced pressure. The crude was purified by silica gel column chromatography with a mixture of petroleum ether, dichloromethane and ethyl acetate (20%, 79%, 1% respectively) as the eluent, then recrystallized from CHCl<sub>3</sub>/MeOH affording 48 mg (63% yield) of **8** as a bright red powder. <sup>1</sup>H NMR (499 MHz, CDCl<sub>3</sub>) δ = 7.50 (d, J = 8.5 Hz, 4H), 7.29 – 7.22 (m, 4H), 7.14 – 6.98 (m, 40H), 4.90 (s, 4H) ppm.

<sup>13</sup>C NMR (125 MHz, CDCl<sub>3</sub>) δ = 162.92, 148.52, 147.21, 143.44, 143.43, 143.12, 142.69, 140.20, 137.65, 131.86, 131.55, 131.48, 131.41, 128.84, 128.57, 128.03, 127.99, 127.82, 127.47, 127.03, 126.88, 126.86, 125.97, 109.73, 45.79 ppm.

HRMS (DCTB, M+) calcd for C<sub>72</sub>H<sub>52</sub>N<sub>2</sub>O<sub>2</sub><sup>+</sup> 976.40259; found 976.40233.

### 4.3 X-Ray structure determinations

Details about data collection and solution refinement are given in Table S1. Single crystals of the compounds were mounted on glass fibre loops using a viscous hydrocarbon oil to coat the crystal and then transferred directly to cold nitrogen stream for data collection. X-ray data collection were performed at 150 K and ambient temperature on an Agilent Supernova with CuKα (λ = 1.54184 Å). The structures were solved by direct methods with the SHELXS-97 and SIR92 programs and refined against all F<sup>2</sup> values with the SHELXL-97 program using the WinGX graphical user interface. All non-H atoms were refined anisotropically. Hydrogen atoms were introduced at calculated positions (riding model), included in structure factor calculations but not refined. Crystallographic data for the two structures have been deposited with the Cambridge Crystallographic Data Centre, deposition numbers CCDC 2237602 (**3RR**) and CCDC 2153712 (**5**). These data can be obtained free of charge from CCDC, 12 Union road, Cambridge CB2 1EZ, UK (e-mail: deposit@ccdc.cam.ac.uk or <http://www.ccdc.cam.ac.uk>).

## Acknowledgements

The authors thank the CNRS, the University of Angers and the RFI Regional project LUMOMAT (grant to M. M. T., project HinTenSiF). Ingrid Freuze (University of Angers) is gratefully acknowledged for MS characterization, and Magali Allain (University of Angers) for help with the X-ray structures. Dr. Kévin Martin (Moltech-Anjou) is thanked for help with the CD characterization and Allan Leroy (ETSCO student) is gratefully acknowledged for his contribution in the synthesis of one enantiomer of compounds **5** and **6**.

## References

1. F. Song, Z. Xu, Q. Zhang, Z. Zhao, H. Zhang, W. Zhao, Z. Qiu, C. Qi, H. Zhang, H. H. Y. Sung, I. D. Williams, J. W. Y. Lam, Z. Zhao, A. Qin, D. Ma and B. Z. Tang, *Adv. Funct. Mater.*, 2018, **28**, 1800051.
2. K. He, S. Zhou, W. Li, H. Tian, Q. Tang, J. Zhang, D. Yan, Y. Geng and F. Wang, *J. Mater. Chem. C*, 2019, **7**, 3656-3664.
3. Q. Liu, S. E. Bottle and P. Sonar, *Adv. Mater.*, 2020, **32**, 1903882.
4. W. W. Bao, R. Li, Z. C. Dai, J. Tang, X. Shi, J. T. Geng, Z. F. Deng and J. Hua, *Front. Chem.*, 2020, **8**, 1-6.
5. M. Mastropasqua Talamo, F. Pop, P. Hume, M. Abbas, G. Wantz and N. Avarvari, *J. Mater. Chem. C*, 2022, **10**, 8034-8042.
6. B. W. H. Saes, M. Lutz, M. M. Wienk, S. C. J. Meskers and R. A. J. Janssen, *J. Phys. Chem. C*, 2020, **124**, 25229-25238.
7. S. Miltzer, N. Nishimura, N. R. Ávila-Rovelo, W. Matsuda, D. Schwaller, P. J. Mésini, S. Seki and A. Ruiz-Carretero, *Chem. Eur. J.*, 2020, **26**, 9998-10004.
8. X. Shang, I. Song, J. H. Lee, M. Han, J. C. Kim, H. Ohtsu, J. Ahn, S. K. Kwak and J. H. Oh, *J. Mater. Chem. C*, 2019, **7**, 8688-8697.
9. J. Roncali, *Macromol. Rapid Commun.*, 2007, **28**, 1761-1775.
10. J. Gierschner, J. Cornil and H.-J. Egelhaaf, *Adv. Mater.*, 2007, **19**, 173-191.
11. H. Han, Y. J. Lee, J. Kyhm, J. S. Jeong, J.-H. Han, M. K. Yang, K. M. Lee, Y. Choi, T.-H. Yoon, H. Ju, S.-k. Ahn and J. A. Lim, *Adv. Funct. Mater.*, 2020, **30**, 2006236.
12. Y. Deng, M. Wang, Y. Zhuang, S. Liu, W. Huang and Q. Zhao, *Light Sci. Appl.*, 2021, **10**, 76.
13. C. Hao, L. Xu, M. Sun, H. Zhang, H. Kuang and C. Xu, *Chem. Eur. J.*, 2019, **25**, 12235-12240.
14. J. Han, S. Guo, H. Lu, S. Liu, Q. Zhao and W. Huang, *Adv. Opt. Mater.*, 2018, **6**, 1800538.
15. F. Pop, N. Zigon and N. Avarvari, *Chem. Rev.*, 2019, **119**, 8435-8478.
16. C. E. Killalea, M. Samperi, G. Siligardi and D. B. Amabilino, *Chem. Commun.*, 2022, **58**, 4468-4471.
17. G. Albano, F. Zinna, F. Urraci, M. A. M. Capozzi, G. Pescitelli, A. Punzi, L. Di Bari and G. M. Farinola, *Chem. Eur. J.*, 2022, **28**, e202201178.
18. G. Pescitelli, L. Di Bari and N. Berova, *Chem. Soc. Rev.*, 2014, **43**, 5211-5233.
19. Y. Nagata and T. Mori, *Front. Chem.*, 2020, **8**, 1-6.
20. H. Kubo, T. Hirose, T. Nakashima, T. Kawai, J.-y. Hasegawa and K. Matsuda, *J. Phys. Chem. Lett.*, 2021, **12**, 686-695.
21. L. Arrico, L. Di Bari and F. Zinna, *Chem. Eur. J.*, 2021, **27**, 2920-2934.
22. F. Zinna, U. Giovanella and L. D. Bari, *Adv. Mater.*, 2015, **27**, 1791-1795.
23. F. Zinna and L. Di Bari, *Chirality*, 2015, **27**, 1-13.
24. K. Dhbaibi, L. Favereau, M. Srebro-Hooper, M. Jean, N. Vanthuyne, F. Zinna, B. Jamoussi, L. Di Bari, J. Autschbach and J. Crassous, *Chem. Sci.*, 2018, **9**, 735-742.
25. T. Gao, Z. Jiang, B. Chen, Q. Sun, Y. Orooji, L. Huang and Z. Liu, *Dyes Pigm.*, 2020, **173**, 107998.

26. A. Taniguchi, D. Kaji, N. Hara, R. Murata, S. Akiyama, T. Harada, A. Sudo, H. Nishikawa and Y. Imai, *RSC Adv.*, 2019, **9**, 1976-1981.
27. F. Zinna, G. Albano, A. Taddeucci, T. Colli, L. A. Aronica, G. Pescitelli and L. Di Bari, *Adv. Mater.*, 2020, **32**, 2002575.
28. J. Wade, J. N. Hilfiker, J. R. Brandt, L. Liirò-Peluso, L. Wan, X. Shi, F. Salerno, S. T. J. Ryan, S. Schöche, O. Arteaga, T. Jávorfí, G. Siligardi, C. Wang, D. B. Amabilino, P. H. Beton, A. J. Campbell and M. J. Fuchter, *Nat. Commun.*, 2020, **11**, 6137.
29. M. Grzybowski, E. Glodkowska-Mrowka, T. Stokłosa and D. T. Gryko, *Org. Lett.*, 2012, **14**, 2670-2673.
30. M. Grzybowski and D. T. Gryko, *Adv. Opt. Mater.*, 2015, **3**, 280-320.
31. M. A. Naik, N. Venkatramaiah, C. Kanimozhi and S. Patil, *J. Phys. Chem. C*, 2012, **116**, 26128-26137.
32. A. Leventis, J. Royakkers, A. G. Rapidis, N. Goodeal, M. K. Corpinot, J. M. Frost, D.-K. Bučar, M. O. Blunt, F. Cacialli and H. Bronstein, *J. Am. Chem. Soc.*, 2018, **140**, 1622-1626.
33. J. Mei, N. L. C. Leung, R. T. K. Kwok, J. W. Y. Lam and B. Z. Tang, *Chem. Rev.*, 2015, **115**, 11718-11940.
34. X. Y. Shen, Y. J. Wang, H. Zhang, A. Qin, J. Z. Sun and B. Z. Tang, *Chem. Commun.*, 2014, **50**, 8747-8750.
35. J. Roose, B. Z. Tang and K. S. Wong, *Small*, 2016, **12**, 6495-6512.
36. C. Shen, F. Gan, G. Zhang, Y. Ding, J. Wang, R. Wang, J. Crassous and H. Qiu, *Mater. Chem. Front.*, 2020, **4**, 837-844.
37. M. Hu, F.-Y. Ye, C. Du, W. Wang, T.-T. Zhou, M.-L. Gao, M. Liu and Y.-S. Zheng, *ACS Nano*, 2021, **15**, 16673-16682.
38. M. Mastropasqua Talamo, F. Pop and N. Avarvari, *Chem. Commun.*, 2021, **57**, 6514-6517.
39. M. Kamioka, Y. Wang, S. Mori, H. Furuta and S. Shimizu, *Eur. J. Inorg. Chem.*, 2022, **2022**, e202200081.
40. A. Punzi, D. Blasi, A. Operamolla, R. Comparelli, G. Palazzo and G. M. Farinola, *RSC Adv.*, 2021, **11**, 11536-11540.
41. C. Adamo and V. Barone, *J. Chem. Phys.*, 1999, **110**, 6158-6170.
42. A. Schäfer, C. Huber and R. Ahlrichs, *J. Chem. Phys.*, 1994, **100**, 5829-5835.
43. M. J. Frisch, G. W. Trucks, H. B. Schlegel, G. E. Scuseria, M. A. Robb, J. R. Cheeseman, G. Scalmani, V. Barone, B. Mennucci, G. A. Petersson, H. Nakatsuji, M. Caricato, X. Li, H. P. Hratchian, A. F. Izmaylov, J. Bloino, G. Zheng, J. L. Sonnenberg, M. Hada, M. Ehara, K. Toyota, R. Fukuda, J. Hasegawa, M. Ishida, T. Nakajima, Y. Honda, O. Kitao, H. Nakai, T. Vreven, J. A. Montgomery Jr., J. E. Peralta, F. Ogliaro, M. Bearpark, J. J. Heyd, E. Brothers, K. N. Kudin, V. N. Staroverov, T. Keith, R. Kobayashi, J. Normand, K. Raghavachari, A. Rendell, J. C. Burant, S. S. Iyengar, J. Tomasi, M. Cossi, N. Rega, J. M. Millam, M. Klene, J. E. Knox, J. B. Cross, V. Bakken, C. Adamo, J. Jaramillo, R. Gomperts, R. E. Stratmann, O. Yazyev, A. J. Austin, R. Cammi, C. Pomelli, J. W. Ochterski, R. L. Martin, K. Morokuma, V. G. Zakrzewski, G. A. Voth, P. Salvador, J. J. Dannenberg, S. Dapprich, A. D. Daniels, O. Farkas, J. B. Foresman, J. V. Ortiz, J. Cioslowski and D. J. Fox, *Gaussian 09, Revision D.01*, Wallingford, CT, 2013.
44. T. Cauchy and B. Da Mota, *Quchemreport. A python program for control quality and automatic generation of quantum chemistry results*, University of Angers, 2020.
45. N. M. O'Boyle, A. L. Tenderholt and K. M. Langner, *J. Comput. Chem.*, 2008, **29**, 839-845.
46. C. Liu, C. Yuan, G. Shi, K. Jia, J. Liu, K.-P. Wang, S. Chen and Z.-Q. Hu, *Dyes Pigm.*, 2023, **210**, 110992.
47. H. Lu, Y. Zheng, X. Zhao, L. Wang, S. Ma, X. Han, B. Xu, W. Tian and H. Gao, *Angew. Chem. Int. Ed.*, 2016, **55**, 155-159.

48. Y.-L. Wang, C. Li, H.-Q. Qu, C. Fan, P.-J. Zhao, R. Tian and M.-Q. Zhu, *J. Am. Chem. Soc.*, 2020, **142**, 7497-7505.
49. R. Tian, Y.-L. Wang, C. Li and M.-Q. Zhu, *Mater. Chem. Front.*, 2022, **6**, 1188-1193.
50. F. Zinna, T. Bruhn, C. A. Guido, J. Ahrens, M. Bröring, L. Di Bari and G. Pescitelli, *Chem. Eur. J.*, 2016, **22**, 16089-16098.